Loading-Mode Dependence of Topology and Functional Grading in TPMS Lattices

Ali Entezari [1]*, Chi Wu [2], Boyang Wan [3], Yuhao Zhang [1], Anson Wen Han Cheong [4], Qing Li [3]*

[1] The School of Electrical, Mechanical and Biomedical Engineering, Faculty of Engineering and Information Technology, University of Technology Sydney, Sydney, NSW 2007, Australia
[2] School of Engineering, University of Newcastle, Callaghan, NSW, 2308, Australia
[3] School of Aerospace, Mechanical and Mechatronic Engineering, The University of Sydney, Sydney, NSW 2006, Australia
[4] School of Mechanical and Manufacturing Engineering, University of New South Wales, Sydney, NSW 2052, Australia

* Corresponding authors; Email: ali.entezari@uts.edu.au; qing.li@sydney.edu.au

Abstract. Additively manufactured triply periodic minimal surface (TPMS) lattices, particularly in their functionally graded (FG) form, offer strong potential for load-bearing biomedical applications due to their tunable mechanical properties and biomimetic architecture. However, their performance is predominantly evaluated under uniaxial compression, leaving their behaviour under more complex loading conditions involving shear and torsion poorly understood. In this work, we present a systematic investigation of the mechanical response of gyroid and primitive FG-TPMS lattices under compression, compression–shear, and torsional loading. Lattices with similar nominal global architectural porosities (approximately 47% for primitive and 45% for gyroid) were fabricated from Digital ABS Plus™ using PolyJet printing and characterised experimentally. The results revealed a strong loading-mode dependence of functional grading and topology. Under compression, grading enhanced stiffness in gyroid lattices but had limited influence on primitive lattices, which consistently exhibited higher compressive stiffness and yield load. Under compression–shear, stiffness and yield showed minimal sensitivity to grading. In contrast, torsional loading exhibited a pronounced dependence on grading, with substantial increases in stiffness and yield torque achieved by redistributing material towards the outer regions. While primitive lattices outperformed gyroid under compression, this advantage did not generalise to shear- or torsion-dominated conditions. These findings demonstrate the loading-mode dependence of radial grading and provide experimental evidence to guide the design of FG-TPMS lattices for specific loading conditions.

Keywords: Triply periodic minimal surface (TPMS); functionally graded lattices; torsional loading; shear loading; additive manufacturing

1. Introduction

Triply periodic minimal surface (TPMS) architectures are mathematically defined porous structures characterised by continuous surfaces with zero mean curvature and periodicity in three dimensions [1-3]. Unlike conventional strut-based lattices, TPMS lattices exhibit smooth, non-self-intersecting geometries

that minimise stress concentrations and enable more uniform load distribution [4]. These features, combined with fully interconnected pore networks, have led to growing interest in TPMS lattices across a wide range of applications, including orthopaedic implants, bone tissue engineering, and other load-bearing biomedical devices [5-8]. In such contexts, TPMS architectures offer a unique combination of high surface area, geometric continuity, and tunable mechanical properties, making them particularly attractive for applications requiring both structural integrity and functional adaptability [9, 10].

Building upon uniform TPMS designs, functionally graded TPMS (FG-TPMS) lattices introduce spatial variations in architectural parameters such as architectural porosity, wall thickness, or unit cell size, enabling location-specific control over mechanical response and permeability [11-16]. This design strategy is often inspired by the hierarchical organisation of natural bone, where a dense cortical shell encloses a more porous cancellous core, resulting in a structure that is both mechanically efficient and lightweight [17, 18]. By incorporating similar gradients, FG-TPMS lattices can achieve gradual stiffness transitions, improved load transfer, and reduced stress shielding compared to uniform designs [19, 20]. Despite these advantages, existing studies have primarily evaluated FG-TPMS lattices under uniaxial compression, and their mechanical behaviour under loading conditions involving significant shear and torsional components remains fundamentally unclear [21-25].

In load-bearing biomedical applications, such as long bone defect reconstruction, spinal interbody fusion, and maxillofacial implants, lattice-based structures are subjected to complex loading environments rather than purely axial compression [26-29]. These loading conditions typically involve combinations of compressive, shear, and torsional forces arising from physiological activities [30]. Under such conditions, the mechanical response of porous structures is governed not only by overall density but also by the spatial distribution of material and its interaction with structural topology [31]. In particular, loading modes that introduce bending and shear-dominated deformation mechanisms can significantly alter stress distribution, failure initiation, and overall load-bearing capacity [32]. Failure to account for these effects may lead to localised stress concentrations and compromised structural performance.

Extensive experimental and computational studies have characterised the compressive stiffness, strength, energy absorption, and deformation behaviour of TPMS lattices [11, 12, 33-40]. Afshar et al. [41], for example, showed that graded TPMS architectures can exhibit markedly different compressive failure modes, with stretching-dominated P-surfaces undergoing layer-by-layer collapse, whereas bending-dominated D-surfaces develop 45° shear bands and, in graded configurations, may exhibit brittle fracture. Similarly, Zhang et al. [42] demonstrated that functional grading modifies these topology-dependent

behaviours, influencing deformation patterns, shear band propagation, and failure localisation. However, these insights are largely derived from uniaxial compression and may lead to suboptimal or even misleading conclusions when applied to real-world loading environments involving significant shear and torsion.

A limited number of studies have explored alternative loading scenarios. Ejeh et al. [43] investigated the flexural behaviour of functionally graded and hybrid TPMS lattices under four-point bending, demonstrating that relative density gradation and topology hybridisation can enhance flexural stiffness and alter failure mechanisms. Similarly, Hailu et al. [44] examined torsional behaviour and showed that tailoring material distribution in accordance with torsional stress fields can improve stiffness and energy absorption. However, these studies remain confined to individual loading modes and do not provide a systematic comparison across different loading conditions. Moreover, the grading strategies employed are predominantly one-dimensional, typically varying along a single axis, and do not capture radially graded architectures that are particularly relevant for cylindrical lattices and biomimetic designs inspired by natural bone. Accordingly, the key question is how radial grading influences the mechanical response of each architecture under compression, compression–shear, and torsion, and whether the effect of grading depends on loading mode.

To address this gap, the present study systematically investigates the mechanical behaviour of functionally graded TPMS lattices under multiple loading conditions, including axial compression, combined compression–shear, and torsion. Two representative TPMS topologies, gyroid and primitive, are considered due to their distinct morphological characteristics and widespread use in lattice design. For each topology, both uniform and radially graded configurations are developed with controlled radial porosity distributions while maintaining similar global architectural porosity (approximately 47% for primitive and 45% for gyroid), enabling direct isolation of grading effects. The lattices are fabricated using high-resolution PolyJet additive manufacturing in Digital ABS Plus™ and experimentally tested under the three loading conditions. This experimental comparison evaluates how radial grading affects stiffness, yield load or yield torque, and observed deformation and failure behaviour, and whether advantages identified under uniaxial compression persist under compression–shear and torsion.

2. Materials and Methods

2.1. Design of FG-TPMS lattices

TPMS architectures were employed to define the internal porous structures. Two representative TPMS geometries, gyroid and primitive, were selected for their distinct morphological characteristics and widespread use in tissue engineering and implantable device applications [6, 45]. As depicted in Figure 1, designs with uniform architectural porosity (P1 and G1), moderate radial grading (P2 and G2), and steep radial grading (P3 and G3) were studied. Their level-set equations were implemented using the Solid Networks setting in MSLattice [45] to generate parent geometries with a diameter of 10 mm and a unit-cell length of 1 mm. In Blender 5.2, each parent geometry was uniformly scaled by a factor of three and trimmed by Boolean intersection with a cylindrical envelope measuring 30 mm in diameter and 30 mm in height. The final unit-cell length was therefore 3 mm, with ten unit cells across the specimen diameter. Pore dimensions reported in Figure 1 refer to the final scaled geometry.

In MSLattice, the interface defined the implicit surface through:

$$F(x, y, z) - C(x, y, z) = 0 \quad (1)$$

Where x, y, and z denote the model-coordinate variables used in the MSLattice input expressions.

The topology functions entered for the primitive and gyroid architectures were:

Primitive: $$F_P(x, y, z) = \cos(2\pi x) + \cos(2\pi y) + \cos(2\pi z) \quad (2)$$

Gyroid: $$F_G(x, y, z) = \sin(2\pi x)\cos(2\pi y) + \sin(2\pi y)\cos(2\pi z) + \sin(2\pi z)\cos(2\pi x) \quad (3)$$

The isovalue functions defining the primitive designs were:

$$C_{P1}(x, y, z) = -0.110 \quad (4)$$

$$C_{P2}(x, y, z) = 0.35 - 0.15\sqrt{x^2 + y^2} \quad (5)$$

$$C_{P3}(x, y, z) = 0.85 - 0.3\sqrt{x^2 + y^2} \quad (6)$$

The isovalue functions defining the gyroid designs were:

$$C_{G1}(x, y, z) = -0.160 \quad (7)$$

$$C_{G2}(x, y, z) = 0.5 - 0.2\sqrt{x^2 + y^2} \quad (8)$$

$$C_{G3}(x, y, z) = 1.15 - 0.4\sqrt{x^2 + y^2} \quad (9)$$

For G2, G3, P2 and P3, the isovalue functions depended on $\sqrt{x^2 + y^2}$ and were independent of z. In the graded designs, architectural porosity decreased and relative density increased from the central axis towards the outer surface.

Figure 1 reports the local porosity, relative-density values, and pore sizes for each design. Architectural porosity, $\emptyset_{arch}$, denotes the volume fraction of void space created by the TPMS architecture, excluding pores within the printed Digital ABS Plus™ material. For the ideal CAD geometry, geometric relative density, ρ_{rel} , represents the solid volume fraction and is complementary to architectural porosity:

$$\rho_{rel} = 1 - \emptyset_{arch} \tag{10}$$

Open or closed pores within the printed material were not quantified in this study.

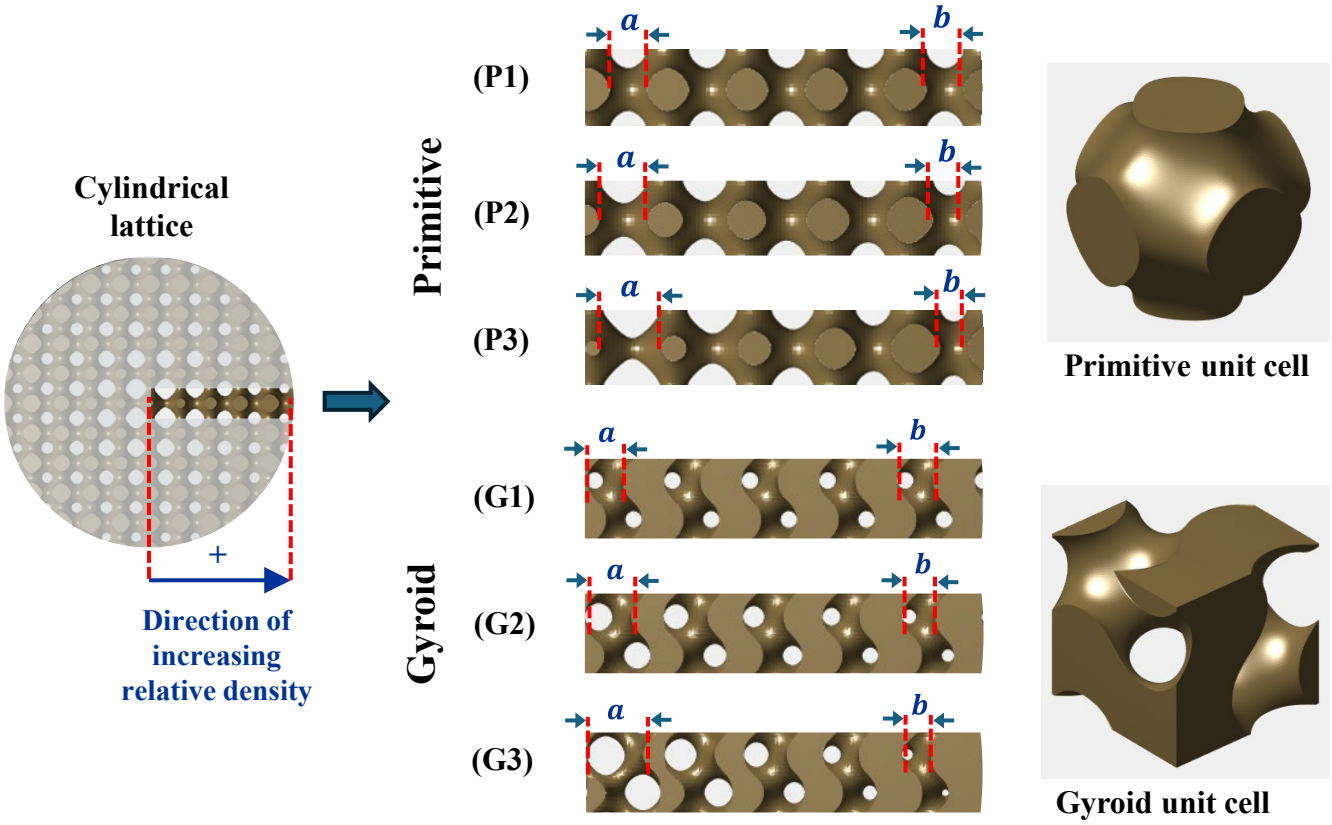

Design	Architectural porosity (%)		Relative density (%)		Pore size (mm)	
	centre	outer surface	centre	outer surface	***a*** (centre)	***b*** (outer surface)
P1	~ 47	~ 47	~ 53	~ 53	1.35	1.35
P2	~ 57	~ 42	~ 43	~ 58	1.71	1.2
P3	~ 67	~ 35	~ 33	~ 65	2.1	0.96
G1	~ 45	~ 45	~ 55	~ 55	1.38	1.38
G2	~ 64	~ 34	~ 36	~ 66	1.77	1.17
G3	~ 80	~ 21	~ 20	~ 79	2.22	0.9

Figure 1. *Design strategy and geometric parameters of the radially graded Gyroid and Primitive lattices. The arrow indicates the direction of increasing relative density from the central axis towards the outer surface. Cross-sectional views show the uniform designs (G1/P1), moderate radial gradients (G2/P2) and steep radial gradients (G3/P3). Three-dimensional renderings illustrate the corresponding unit cells. The table reports approximate architectural porosity and relative density at the centre and outer surface, together with pore sizes a (centre) and b (outer surface). All designs have a final unit-cell length of 3 mm.*

The radial grading was qualitatively inspired by the organisation of bone in regions where a relatively dense cortical shell surrounds a more porous trabecular interior. For quantitative context, Sadoughi et al. [46] reported mean human trabecular bone volume fractions (BV/TV) of approximately 12% in the proximal tibia, 11% in the greater trochanter, and 25% in the femoral neck. For human femoral cortical

bone, Stein et al. [47] reported a median intracortical porosity of 5.9%, measured as the proportion of cortical cross-sectional area occupied by pores.

Nominal global architectural porosity was approximately 47% for primitive and 45% for gyroid lattices, corresponding to geometric relative densities of approximately 53% and 55%, respectively. The graded designs spanned local relative densities of approximately 43–58% for P2, 33–65% for P3, 36–66% for G2, and 20–79% for G3, increasing from the central axis towards the outer surface (Figure 1). Global relative density was maintained approximately constant across the uniform and graded designs within each topology, allowing the effects of radial material redistribution to be investigated at similar total material content. These density levels served as controlled experimental design conditions rather than anatomical density targets.

The nominal global relative densities exceed the mean trabecular BV/TV values reported in the literature [46, 47]. The biological inspiration therefore concerns the spatial organisation of material rather than reproduction of absolute anatomical values or the full trabecular-to-cortical density contrast. The study investigated how this bone-inspired grading, implemented at selected architectural porosity levels, influences mechanical response under different loading conditions. This approach may inform the tailoring of lattice mechanical behaviour for load-bearing implants and other engineering applications. Differences in architecture, length scale and measurement method limit direct comparisons with natural bone, and biological performance was not evaluated.

2.2. Fabrication of lattice specimens

The lattice specimens were fabricated using a Stratasys J750 PolyJet™ 3D printer (Stratasys Ltd., USA) in High Mix mode, with a nominal build layer thickness of 27 μm. All designs were exported as STL files and processed using the manufacturer's proprietary software prior to printing. The specimens were printed upright, with their longitudinal axes parallel to the build direction (Z-axis) and perpendicular to the build plate.

The lattices were manufactured using Digital ABS Plus™, a photopolymer formulated to simulate the mechanical behaviour of conventional ABS. Manufacturer-reported properties include an elastic modulus of 2.6–3.0 GPa and tensile strength of 55–60 MPa. These values describe the printed bulk material and were not independently measured in this study.

Following printing, support material was removed using a cleaning bath prepared from 20 L of water, 200 g of sodium metasilicate and 400 g of sodium hydroxide. Cleaning was conducted for 8 h per day over

three days, giving a total processing time of approximately 24 h. At approximately 4 h intervals, the specimens were removed from the bath and rinsed under running tap water to dislodge loosened support material before being returned to the bath. Following support removal, the specimens were soaked in water for approximately 2 h to remove residual cleaning solution.

Following fabrication, the diameter, height, and mass of each specimen were measured to quantify the as-built geometry and estimate apparent density and architectural porosity. The cylindrical envelope volume was calculated as

$$V_{env} = \frac{\pi D^2 H}{4} \tag{11}$$

and the apparent density was calculated as:

$$\rho_{app} = \frac{m_{meas}}{V_{env}} \tag{12}$$

Relative density and architectural porosity were then calculated as:

$$\rho_{rel}(\%) = 100\frac{\rho_{app}}{\rho_{material}} = 100\frac{m_{meas}}{\rho_{material} V_{env}} \tag{13}$$

$$Ø_{arch}(\%) = 100 - \rho_{rel}(\%) \tag{14}$$

where $\rho_{material} = 1.17\ g/cm^3$ was taken from the manufacturer-reported density of Digital ABS Plus™. Three specimens were measured for each configuration, and values are reported as mean ± SD. The mass-based estimate of architectural porosity assumes that the printed material has the manufacturer-reported density. This method does not independently distinguish architectural voids from any pores within the printed material.

2.3. Experimental mechanical characterisation

Compression and compression–shear tests were conducted using an MTS 810 Material Test System fitted with a Model 661.22D-01 force transducer (250 kN capacity; 0.5% measurement accuracy). Torsion tests were conducted using an ElectroForce TA 3550 system fitted with a TA ElectroForce Model 1216FSG-15kN axial–torsion transducer (15 kN axial capacity; 140 N·m torque capacity). The transducer label did not specify measurement accuracy. Custom-designed jigs were used for the three loading scenarios shown in Figure 2. Torque was measured using the axial–torsion transducer, and rotation was recorded by the ElectroForce TA 3550 system to obtain the torque–rotation response. For uniaxial compression tests, the lattice specimens were placed between two flat steel plates and loaded along their longitudinal axis (Figure 2a). All tests were conducted under displacement control at a crosshead speed of 1 mm/min.

To investigate combined compression-shear loading conditions, a customised fixture with a 45° inclined interface was designed to introduce both compressive and shear components simultaneously (Figure 2b). Under ideal geometric decomposition, the 45° fixture orientation corresponds to equal nominal axial (compressive) and transverse (shear) components of the applied force. This describes the external loading direction and does not imply equal or spatially uniform stresses within the lattice. To prevent specimen slippage during loading, cylindrical recesses (2 mm depth) with a profile matching the specimen were incorporated into both sides of the fixture. Tests were performed under displacement control at a crosshead speed of 1 mm/min.

Torsional behaviour was evaluated using a pair of custom-designed jigs (Figure 2c) with cubic pockets with a depth of 5 mm to securely grip the lattice ends. To facilitate this, the cylindrical lattices were designed with integrated cubic end sections (5 mm in height) at both ends, which were printed as part of the specimen to ensure proper engagement with the fixture. The reported overall specimen height was 30 mm, including the two integrated cubic end sections, each 5 mm high. Torsion tests were conducted under rotational control at a constant rate of 30 deg/min.

In the load–displacement and torque–rotation responses, a small initial nonlinear region was occasionally observed, particularly in torsion and compression–shear tests. This region was attributed to the initial settling and alignment of the test fixtures and specimens, and was excluded from the analysis. The linear-elastic segment of each response was selected manually by visual inspection, excluding the initial seating region and subsequent nonlinear behaviour. A linear regression was fitted to this segment, and apparent stiffness was calculated from its slope. For yield determination, the percentage deviation from the fitted response was calculated at each displacement or rotation beyond the fitted linear-elastic interval as:

$$D_i = \frac{|R_{meas,i} - R_{fit,i}|}{|R_{fit,i}|} \times 100\% \qquad (15)$$

where $R_{meas,i}$ is the measured force or torque, and $R_{fit,i}$ is the response predicted by the fitted line at the same displacement or rotation. The operational yield point was defined as the first point at which D_i exceeded 5%; the corresponding force or torque was reported as the yield load or yield torque, respectively. The same fitting and deviation procedure was applied to the compression, compression–shear, and torsion tests. The 5% threshold was adopted as a pragmatic operational cutoff to provide a consistent quantitative definition of yield across loading modes, rather than relying on the first visually apparent departure from linearity. Machine and fixture compliance was not independently calibrated or corrected; therefore, the reported stiffness values are apparent stiffness values and may include

deformation of the testing systems and fixtures. For each lattice configuration and loading condition, three specimens (n=3) were tested, and the results were reported as mean values ± standard deviation.

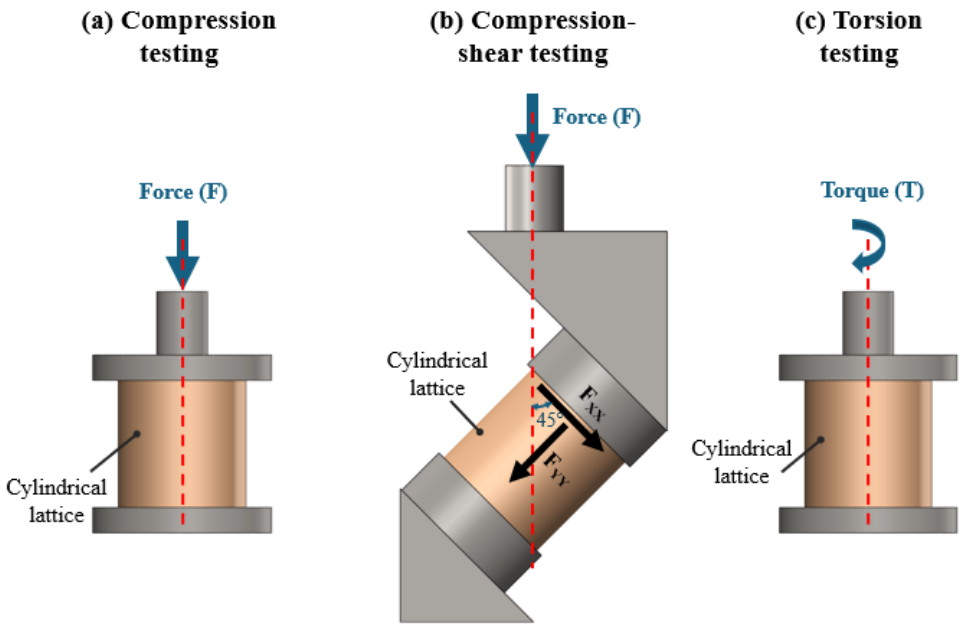

Figure 2. *Schematic representation of the experimental setups used for mechanical characterisation of the TPMS lattices under different loading conditions. (a) uniaxial compression, where the lattice is loaded between two flat plates along its longitudinal axis; (b) compression–shear loading using a customised fixture with a 45° inclined interface, resulting in simultaneous normal (compressive) and shear force components acting on the lattices; and (c) torsional loading, where torque is applied about the longitudinal axis using custom-designed jigs to securely grip the specimen ends.*

2.4. Statistical analysis

Values are reported as mean ± SD ($n = 3$ independent specimens per design). Because the primary aim of the study was to assess the effect of grading within each topology, and nominal architectural porosity was matched across grading levels within, but not between, the topologies (approximately 47% for primitive and 45% for gyroid), the primary grading comparisons were performed using separate one-way ANOVAs within each topology and loading condition, followed by Tukey's multiple-comparisons test. The significance annotations in Figures 6 and 7 reflect these analyses.

As a secondary analysis, separate two-way ANOVAs were performed for each mechanical response and loading condition, with topology, grading, and their interaction as factors. Sidak-adjusted comparisons between the tested topology–porosity configurations were performed at each grading level. Because global architectural porosity differed between the topology groups, cross-topology results describe the tested

topology–porosity configurations and do not isolate the effect of topology from that of relative density. Given the limited sample size ($n = 3$ per design), these secondary results should be interpreted cautiously, and non-significant findings should not be considered evidence of equivalence. Analyses were performed using GraphPad Prism (GraphPad Software, USA).

Differences were considered statistically significant at $p < 0.05$. Levels of statistical significance are indicated as follows: *$p < 0.05$, **$p < 0.01$, ***$p < 0.001$, and ****$p < 0.0001$.

3. Results and Discussion

3.1. Geometrical and fabrication validation of TPMS lattices

Figure 3 shows the geometrical configurations of the designed TPMS lattices, including isometric views and transverse and longitudinal cross-sections for both gyroid and primitive architectures. The uniform designs exhibit a consistent pore morphology, whereas the graded lattices show a radial transition from larger pores in the core to smaller pores towards the periphery.

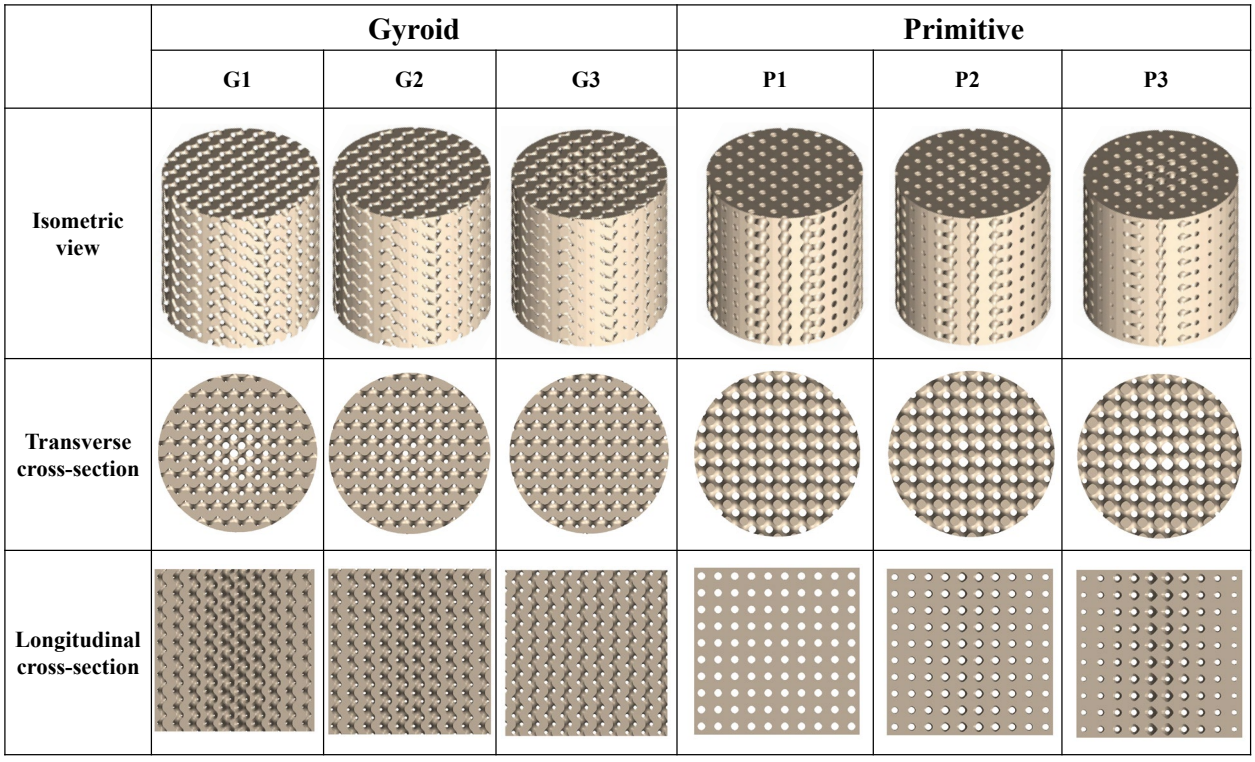

Figure 3. *Representative geometries of cylindrical TPMS lattices with uniform and radially graded architectures. Gyroid (G1–G3) and primitive (P1–P3) lattices are shown on the left and right, respectively. The rows show isometric views (top), transverse cross-sections (middle), and longitudinal cross-sections (bottom). G1 and P1 have uniform architectural porosity, G2 and P2 have moderate radial porosity gradients, and G3 and P3 have steep radial porosity gradients.*

Following the design of the TPMS architectures, the lattices were fabricated using Digital ABS Plus™. Figure 4 presents the as-fabricated specimens, showing both top and isometric views of all lattice configurations. The fabricated lattices reproduced the overall intended geometry and showed no visible structural collapse or major defects.

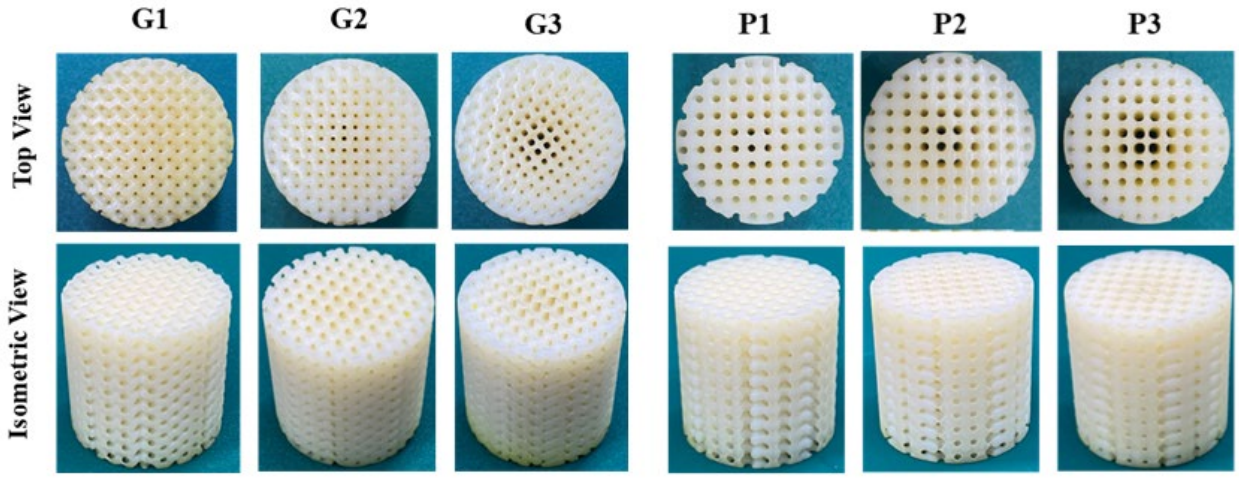

Figure 4. *As-fabricated TPMS lattices produced using PolyJet™ additive manufacturing with Digital ABS Plus™. Top and isometric views are shown for all lattice configurations, including gyroid (G1–G3) and primitive (P1–P3) architectures. For each topology, three designs are presented: a uniform lattice and two functionally graded lattices with moderate and steep radial porosity gradients.*

Measured specimen dimensions and mass, calculated apparent density, and mass-based estimates of relative density and architectural porosity are summarised in Table 1. Across the six configurations, the mean measured diameters and heights each ranged from 30.01 to 30.03 mm, compared with nominal CAD dimensions of 30.0 mm. The differences between the group-mean dimensions and the nominal values were therefore 0.01–0.03 mm, corresponding to approximately 0.03–0.10%.

The estimated as-built relative density was consistently slightly lower than the nominal CAD relative density. For the primitive designs, estimated relative density ranged from approximately 51.5% to 51.8%, compared with nominal values of approximately 53.1–53.2%. For the gyroid designs, the corresponding values were approximately 53.5–53.9% and 55.1–55.2%, respectively. These differences correspond to increases in estimated architectural porosity of approximately 1.3–1.7 percentage points relative to the CAD values. They may reflect fabrication-related deviations in feature dimensions, together with uncertainty associated with using the manufacturer-reported material density in the mass-based calculations. The measurements characterise external dimensional accuracy and global material content; local pore dimensions, wall thickness and surface roughness were not quantitatively assessed.

Table 1. *CAD-designed and as-built properties of the primitive (P1–P3) and gyroid (G1–G3) TPMS specimens. CAD columns show the designed dimensions and nominal relative density and architectural porosity. As-built columns report measured dimensions and mass, apparent density, relative density and architectural porosity as mean ± SD (n=3)*

	Diameter (mm)			Height (mm)			Mass (g)		Apparent density (g/cm3)		Relative density (%)			Architectural porosity (%)		
	CAD	As-built		CAD	As-built		As-built		As-built		CAD	As-built		CAD	As-built	
		Mean	SD		Mean	SD	Mean	SD	Mean	SD		Mean	SD		Mean	SD
P1	30.0	30.03	0.01	30.0	30.02	0.00	12.81	0.02	0.603	0.0011	53.15	51.52	0.09	46.85	48.48	0.09
P2	30.0	30.02	0.01	30.0	30.03	0.01	12.90	0.03	0.607	0.0017	53.20	51.81	0.15	46.80	48.19	0.15
P3	30.0	30.01	0.02	30.0	30.03	0.05	12.83	0.01	0.604	0.0017	53.13	51.63	0.14	46.87	48.37	0.14
G1	30.0	30.03	0.01	30.0	30.02	0.01	13.31	0.03	0.626	0.0013	55.19	53.54	0.11	44.81	46.46	0.11
G2	30.0	30.01	0.02	30.0	30.03	0.01	13.37	0.03	0.630	0.0016	55.11	53.86	0.14	44.89	46.14	0.14
G3	30.0	30.03	0.01	30.0	30.01	0.01	13.35	0.02	0.629	0.0009	55.17	53.73	0.07	44.83	46.27	0.07

3.2. Mechanical performance under axial and multi-axial loading

3.2.1. Overall mechanical response under different loading modes

The global mechanical response of the TPMS lattices under uniaxial compression, compression–shear, and torsional loading is presented in Figure 5. The force–displacement and torque–rotation curves provide an overview of the deformation behaviour of both gyroid (G1–G3) and primitive (P1–P3) architectures prior to detailed quantitative analysis.

Under uniaxial compression, all lattices exhibit an initial linear elastic region followed by a smooth transition into a post-yield regime. Beyond yielding, the structures continue to sustain increasing load with increasing displacement, indicating stable deformation without catastrophic failure. This behaviour is characteristic of progressive collapse and densification of the porous architecture.

In contrast, under compression–shear loading, the response exhibits a small initial nonlinear region associated with fixture compliance and contact establishment, followed by an approximately linear increase in load up to ~2000 N. Beyond this regime, the response becomes nonlinear, reaching a peak load followed by an abrupt drop corresponding to structural failure.

Under torsional loading, torque increases with rotation until a peak is reached, followed by a sharp reduction associated with fracture. Similar to compression–shear loading, failure is localised and

catastrophic; however, the torsional response exhibits more limited plastic deformation prior to fracture, indicating a more abrupt structural collapse.

Across all loading modes, differences between the tested lattice configurations are evident in the shape and progression of the curves. The following quantitative analyses focus first on grading effects within each topology; the response to grading varies with loading mode. Between-topology differences are treated as secondary comparisons of the tested design families because their global porosities were not identical.

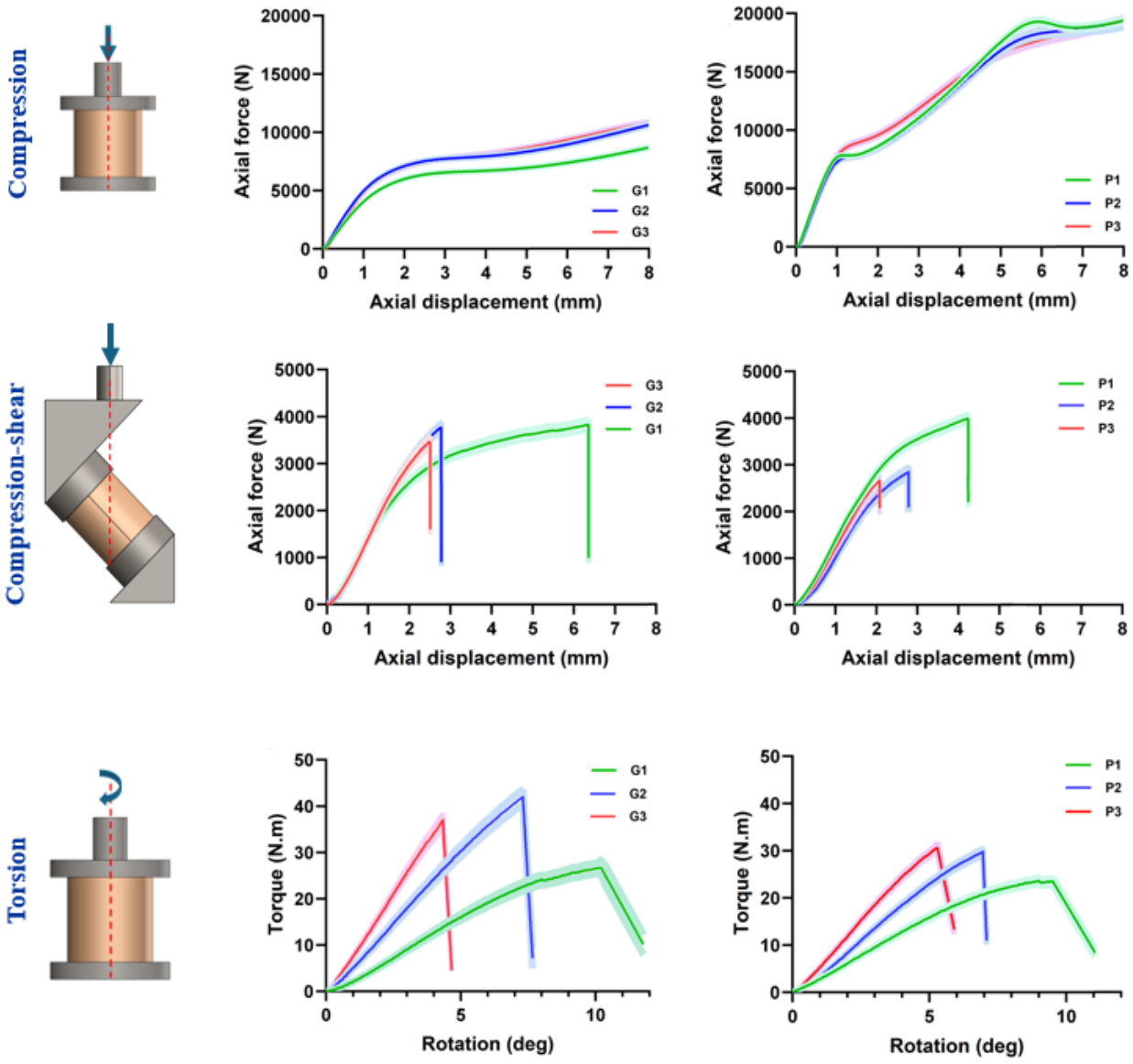

Figure 5. *Mechanical response of TPMS lattices under multi-axial loading. Force–displacement curves under uniaxial compression (top) and compression–shear (middle), and torque–rotation curves under torsion (bottom) for gyroid (G1–G3, left column) and primitive (P1–P3, right column) lattices. Under compression, all lattices exhibit*

stable post-yield deformation with continued load-carrying capacity. In contrast, compression–shear and torsional loading are characterised by a peak response followed by a sharp drop, indicating the onset of structural failure. Differences in the shape and progression of the curves highlight the influence of lattice topology and functional grading on the overall mechanical behaviour.

3.2.2. Stiffness under simple and complex stress states

Stiffness under uniaxial compression.

Under uniaxial compression, gyroid lattices exhibited a clear increase in stiffness with increasing gradient magnitude (Figure 6). Both G2 and G3 showed significantly higher stiffness than the uniform design G1, while no statistically significant difference was observed between G2 and G3, indicating a plateau in compressive stiffness beyond moderate grading. This trend is consistent with previous studies showing that radially graded gyroid structures can exhibit higher compressive stiffness than uniform counterparts at similar porosity levels [48]. In contrast, primitive lattices showed only a weak dependence on grading, with a statistically significant difference observed only between P2 and P3, while the overall variation across P1–P3 remained small. Across the tested designs, primitive lattices exhibited substantially higher compressive stiffness (~9,000–9,500 N/mm) than gyroid lattices (~4,800–5,700 N/mm). Notably, this difference was observed despite the primitive designs having slightly higher global porosity (~47%) than the gyroid designs (~45%). As increased porosity would generally be expected to reduce stiffness, the higher stiffness of the primitive lattices cannot be explained by a higher relative density. This finding therefore supports a strong contribution of lattice architecture to the compressive response.

When expressed in terms of effective modulus, the measured stiffness values correspond to approximately 200–240 MPa for gyroid lattices and 380–400 MPa for primitive lattices. These values fall within the broad range reported for cancellous bone [49, 50].

Stiffness under compression-shear. Under combined compression–shear loading, the influence of functional grading was minimal for both architectures (Figure 6). Gyroid lattices exhibited stiffness values in the range of ~1,700–1,950 N/mm, with a modest increase from G1 to G2 followed by a slight reduction in G3, while primitive lattices (P1–P3) showed nearly identical stiffness (~1,500 N/mm) with no statistically significant differences between configurations. Gyroid lattices exhibited significantly higher stiffness than primitive lattices at moderate and steep grading, whereas the uniform designs did not differ significantly (Section 3.2.4).

The measured stiffness values under compression-shear fall within the range reported for lumbar intervertebral fusion devices [51], suggesting that the proposed designs provide mechanically relevant performance under combined loading conditions.

Stiffness under torsion. In contrast to compression and compression–shear, torsional loading exhibited a strong dependence on functional grading (Figure 6). For both gyroid and primitive lattices, torsional stiffness increased progressively with gradient magnitude, with statistically significant differences observed between configurations. Gyroid lattices increased from ~4 N·m/deg (G1) to ~9 N·m/deg (G3), while primitive lattices increased from ~3 N·m/deg (P1) to ~6 N·m/deg (P3).

These results suggest that redistributing material towards the lattice periphery improves torsional resistance at approximately constant global relative density within each topology. Gyroid lattices exhibited significantly higher torsional stiffness than primitive lattices at all three grading levels (Section 3.2.4). The lower nominal global porosity of gyroid lattices may have contributed to these differences, which cannot be attributed exclusively to topology.

The measured torsional stiffness values of the FG-TPMS lattices fall within the range reported for lumbar intervertebral fusion devices [51], indicating that functional grading provides an effective strategy for tuning torsional performance within clinically relevant limits.

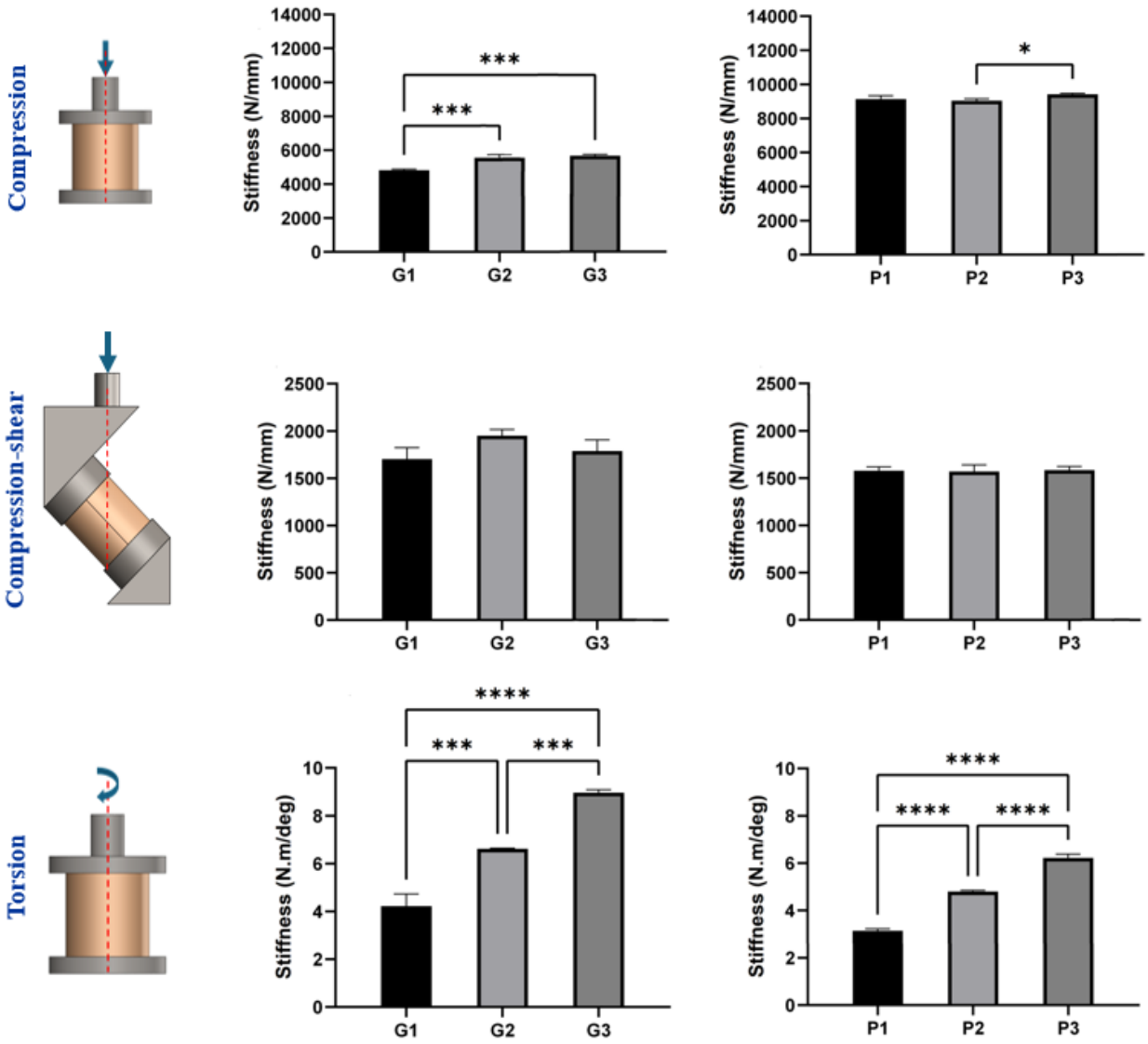

Figure 6. *Mechanical stiffness of gyroid (G1–G3) and primitive (P1–P3) TPMS lattices under uniaxial compression (top row), compression–shear (middle row), and torsion (bottom row). Gyroid and primitive results are shown in the left and right plots, respectively. Each topology includes a uniform design (G1/P1) and designs with moderate (G2/P2) and steep (G3/P3) radial porosity gradients. Bars represent mean ± standard deviation (n = 3 independent specimens per configuration and loading mode). Within-topology differences were assessed using one-way ANOVA followed by Tukey's multiple-comparisons test. Asterisks indicate statistically significant differences between the connected groups: *p < 0.05, ***p < 0.001, and ****p < 0.0001. Comparisons without asterisks were not statistically significant.*

3.2.3. Yield load (compression and compression–shear) and yield torque (torsion)

Following the stiffness response, the yield behaviour of the TPMS lattices under compression, compression–shear, and torsion is presented in Figure 7. The grading response in yield load and yield torque was evaluated within each topology for compression, compression–shear, and torsion (Figure 7).

The within-topology grading comparisons are the primary results; secondary between-topology contrasts are summarised separately in section 3.2.4 below.

Yield load under uniaxial compression. Under uniaxial compression, gyroid lattices showed a modest increase in yield load with increasing gradient magnitude, although the differences between configurations were not statistically significant. Primitive lattices exhibited consistently higher yield loads (~6,000–6,300 N) than gyroid lattices (~3,400–3,800 N), with a relatively slight increase observed between P2 and P3, indicating a limited influence of grading on yield behaviour. When normalised by cross-sectional area, the corresponding compressive yield stress for primitive lattices was approximately ~9 MPa, within the strength range reported for cancellous bone [49, 50].

Yield load under compression–shear. Under combined compression–shear loading, yield load showed minimal variation across graded configurations for both topologies, with no statistically significant differences between grading levels within either topology. Gyroid lattices exhibited a slight increase from G1 to G2 followed by a plateau or marginal decrease at G3, while primitive lattices showed a small reduction with increasing grading. Consistent with the stiffness results, gyroid lattices exhibited higher yield loads than primitive lattices at moderate and steep grading, whereas the uniform designs did not differ significantly (Section 3.2.4). However, the lower nominal global porosity of gyroid lattices (approximately 45% versus 47% for primitive) may have contributed to these differences, preventing attribution exclusively to topology. The measured yield loads (>2,000 N) fall within the range reported for lumbar intervertebral fusion devices [51], indicating mechanically relevant performance under combined loading.

Yield torque under torsion. In contrast, torsional loading exhibited a strong dependence on functional grading, with yield torque increasing systematically with gradient magnitude for both architectures. Statistically significant differences were observed between configurations, with both gyroid and primitive lattices showing substantial improvements from uniform to graded designs. The increase in yield torque indicates that radial material redistribution can improve torsional load-bearing capacity for the tested architectures.

Gyroid lattices exhibited higher yield torque than primitive lattices at moderate and steep grading, whereas the uniform designs did not differ significantly (Section 3.2.4). As noted above, the lower nominal global porosity of gyroid lattices may have contributed to these differences, which cannot be attributed exclusively to topology.

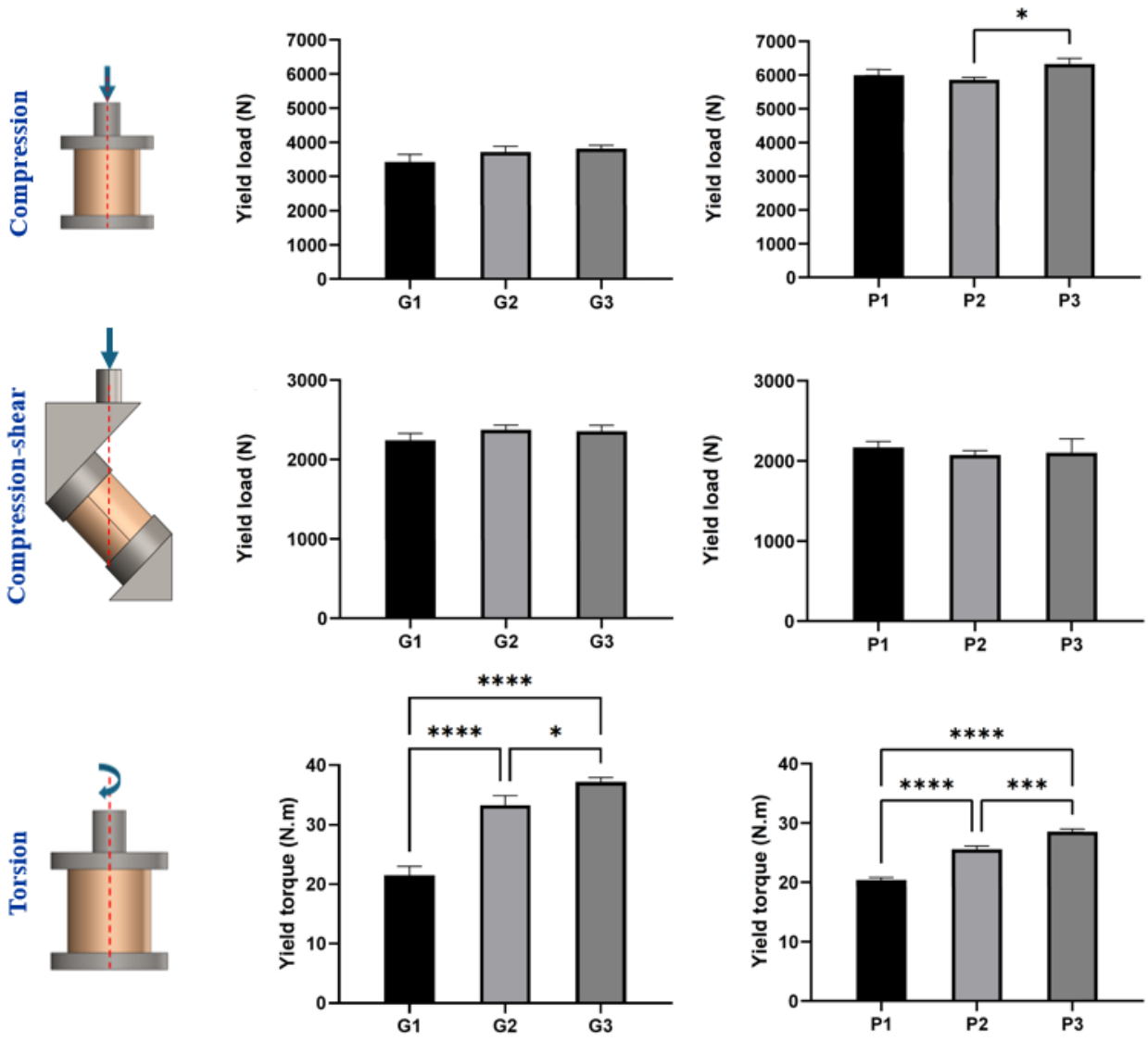

Figure 7. *Yield load and torque of TPMS lattices under multi-axial loading. Yield load under uniaxial compression (top row) and compression–shear (middle row), and yield torque under torsion (bottom row) for gyroid (G1–G3, left column) and primitive (P1–P3, right column) lattices. Data are presented as mean ± standard deviation (n = 3). Statistical significance is indicated as *p < 0.05, ***p < 0.001, and ****p < 0.0001.*

3.2.4. Secondary topology-by-grading analysis

Separate two-way ANOVAs were performed for each response and loading mode, with the topology, grading, and interaction terms summarised in Table 2. These analyses were secondary to the within-topology one-way analyses presented in Figures 6 and 7. Significant topology × grading interactions were observed for compression stiffness ($F(2,12) = 15.94,\ p = 0.0004$), torsional stiffness ($F(2,12) = 20.22,\ p = 0.0001$), and torsional yield torque ($F(2,12) = 24.98, p < 0.0001$). The interactions were not significant for compression yield load ($p = 0.0734$), compression–shear stiffness ($p = 0.0550$), or

compression–shear yield load ($p = 0.1345$). The grading main-effect terms are reported as part of each model but are not used to infer a common grading effect across the two topologies.

Table 2. *Secondary two-way ANOVA results for each response and loading mode.*

Response	Topology	Grading	Topology × grading
Compression stiffness	$F(1,12) = 4026$; $p < 0.0001$	$F(2,12) = 29.79$; $p < 0.0001$	$F(2,12) = 15.94$; $p = 0.0004$
Compression yield load	$F(1,12) = 1078$; $p < 0.0001$	$F(2,12) = 8.971$; $p = 0.0041$	$F(2,12) = 3.272$; $p = 0.0734$
Compression–shear stiffness	$F(1,12) = 36.08$; $p < 0.0001$	$F(2,12) = 3.157$; $p = 0.0791$	$F(2,12) = 3.729$; $p = 0.0550$
Compression–shear yield load	$F(1,12) = 21.52$; $p = 0.0006$	$F(2,12) = 0.1114$; $p = 0.8955$	$F(2,12) = 2.382$; $p = 0.1345$
Torsional stiffness	$F(1,12) = 307$; $p < 0.0001$	$F(2,12) = 442.3$; $p < 0.0001$	$F(2,12) = 20.22$; $p = 0.0001$
Torsional yield torque	$F(1,12) = 150.7$; $p < 0.0001$	$F(2,12) = 222.4$; $p < 0.0001$	$F(2,12) = 24.98$; $p < 0.0001$

Each cell contained $n = 3$ independent specimens. Values are F statistics with numerator and denominator degrees of freedom and omnibus p values. Within each response model, Sidak adjustment was applied to the three topology comparisons across the grading levels. Because the topology groups differed in global porosity, topology terms and grade-specific comparisons represent the tested topology–porosity configurations rather than isolating the effect of topology from relative density.

Sidak-adjusted comparisons between the tested configurations at each grading level showed that primitive lattices had higher compression stiffness and compression yield load than gyroid lattices at all three grading levels (adjusted $p < 0.0001$ for all comparisons). Under compression–shear loading, gyroid lattices had higher stiffness at moderate (adjusted $p = 0.0003$) and steep (p=0.0346) grading, but not under the uniform condition ($p = 0.2505$). Gyroid lattices also had higher compression–shear yield load at moderate ($p = 0.0071$) and steep ($p = 0.0197$) grading, whereas the uniform designs did not differ significantly ($p = 0.7537$). Under torsion, gyroid lattices had higher stiffness at uniform ($p = 0.0003$), moderate ($p < 0.0001$), and steep ($p < 0.0001$) grading. Gyroid lattices also had higher yield torque at moderate and steep grading (both $p < 0.0001$), whereas the uniform designs did not differ significantly ($p = 0.4882$). These secondary comparisons describe the tested topology–porosity configurations and should not be interpreted as isolated effects of topology.

3.2.5. Deformation and failure mechanisms

The post-yield deformation and failure behaviour of the TPMS lattices under different loading conditions are presented in Figures 8–10.

Figure 8 shows the lattices after yielding under uniaxial compression. For all FG configurations, both gyroid and primitive lattices exhibited stable deformation without catastrophic fracture, maintaining structural integrity beyond the onset of yielding. This is consistent with the corresponding force–displacement curves (Figure 5), which showed an initial linear elastic response followed by a plateau associated with progressive collapse of the porous architecture, and a subsequent increase in load at higher strains due to densification.

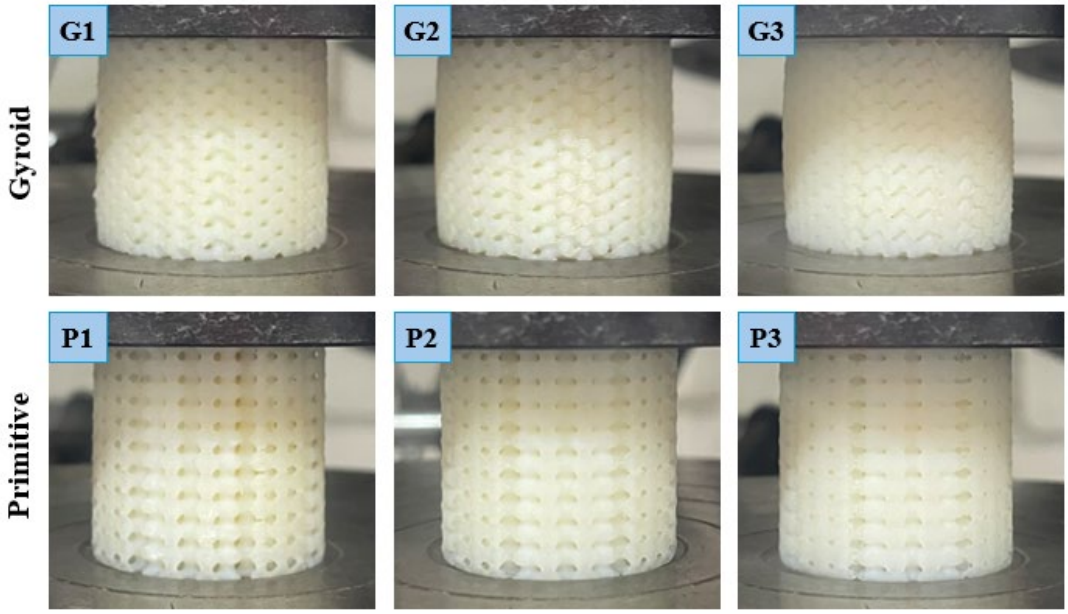

Figure 8. *Post-yield deformation of TPMS lattices under uniaxial compression. Representative images of gyroid (G1–G3) and primitive (P1–P3) lattices after yielding during compression testing. All lattices exhibit stable deformation without catastrophic fracture, maintaining structural integrity beyond the initial yield point.*

In contrast, Figure 9 illustrates the failure behaviour under compression–shear loading, characterised by more localised deformation and pronounced fracture. The dashed orange lines indicate the observed fracture paths, while the red arrows denote the likely locations of fracture initiation. Fracture paths are predominantly inclined, forming diagonal shear bands that appear to originate near opposing lattice corners and extend across the structure.

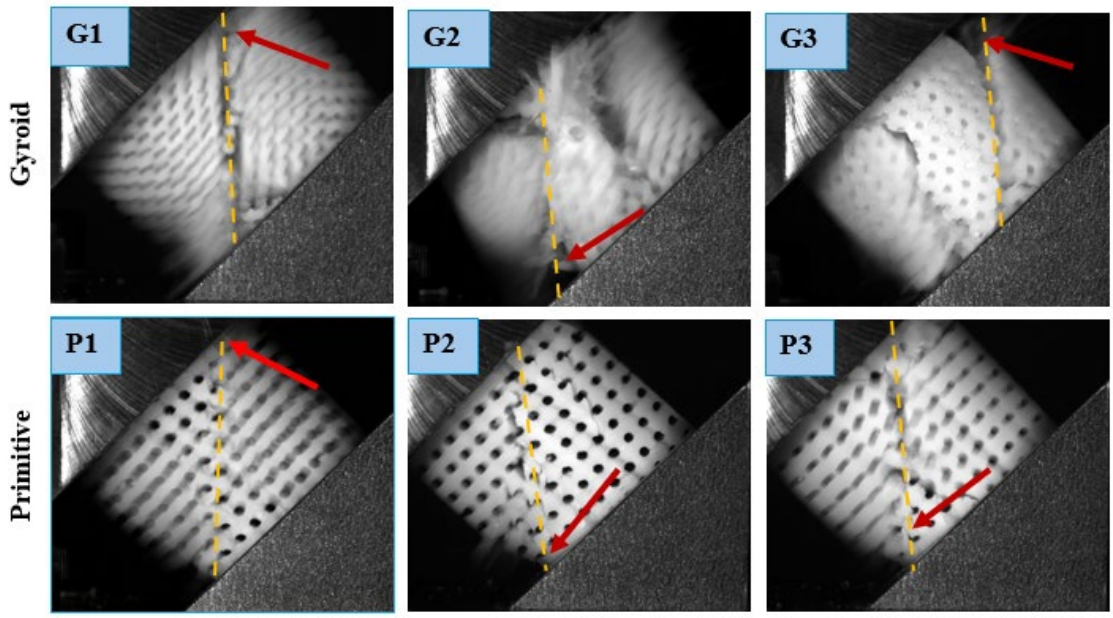

Figure 9. *Failure behaviour of TPMS lattices under compression–shear loading. Representative images of gyroid (G1–G3) and primitive (P1–P3) lattices during compression–shear testing. The dashed orange lines indicate the observed fracture paths, while the red arrows denote the likely locations of fracture initiation.*

Under torsional loading (Figure 10), the lattices exhibited localised fracture with oblique surface crack paths. The dashed orange lines indicate the observed fracture paths, while the red arrows denote the likely locations of fracture initiation. This abrupt failure behaviour is consistent with the sharp drops observed in the torque–rotation curves (Figure 5).

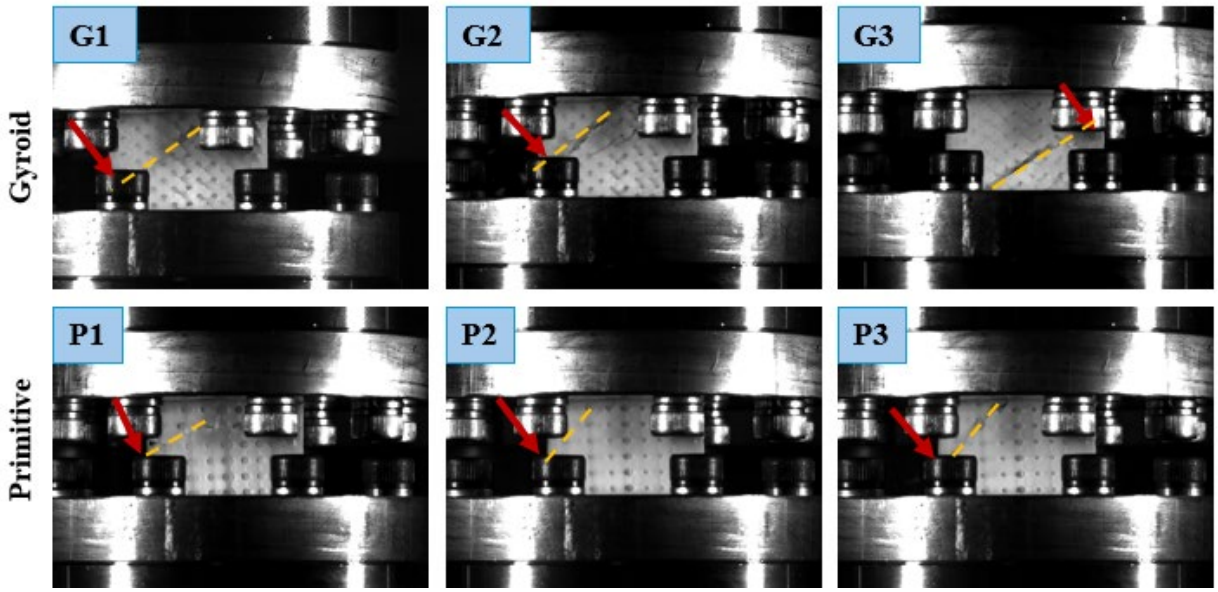

Figure 10. *Failure behaviour of TPMS lattices under torsional loading. Representative images of gyroid (G1–G3) and primitive (P1–P3) lattices during torsion testing. The dashed orange lines indicate the observed fracture paths, while the red arrows denote the likely locations of fracture initiation.*

Despite the insights provided, several limitations should be acknowledged. The present study is based on polymeric specimens fabricated using Digital ABS Plus™, and therefore the absolute mechanical properties may differ from those of metallic or ceramic TPMS lattices commonly used in clinical applications. The bulk-material properties and their dependence on printing orientation were not independently characterised. The experimental evaluation is limited to quasi-static loading, whereas in vivo conditions may involve cyclic and fatigue loading. Furthermore, the sample size for each configuration was limited (n = 3), which may affect the statistical power in detecting subtle differences between groups. Machine and fixture compliance was not independently calibrated or corrected; therefore, the reported stiffness values may include deformation of the testing systems and fixtures. Because fixture compliance may differ among the loading configurations, stiffness results should be interpreted primarily within each loading mode, and cross-mode comparisons should be made cautiously. The primitive and gyroid groups also had slightly different global porosities (approximately 47% and 45%, respectively). Therefore, observed differences between the two architectures cannot be attributed exclusively to topology, as relative density may also have contributed to their mechanical response. Cross-topology comparisons should consequently be interpreted as comparisons between the specific topology–porosity configurations investigated in this study. Future density-matched comparisons would be required to isolate the effect of topology more directly. Future work should evaluate additional materials, fatigue behaviour and more physiologically representative loading conditions.

4. Conclusion

This study experimentally investigated the mechanical behaviour of additively manufactured functionally graded TPMS lattices under compression, combined compression–shear, and torsional loading. The results demonstrated that the effects of radial grading on stiffness and yield behaviour depend on the loading mode. Under uniaxial compression, functional grading enhanced stiffness in gyroid lattices but had limited influence on yield behaviour, while primitive lattices consistently exhibited higher stiffness and yield load within the tested configurations. Under compression–shear, both stiffness and yield showed minimal sensitivity to grading for either topology. In contrast, torsional loading exhibited a pronounced dependence on radial grading, with substantial increases in stiffness and yield torque for both architectures as material was redistributed towards the lattice periphery. Across the tested topology–porosity configurations, the

relative mechanical performance varied with loading mode, highlighting that advantages observed under uniaxial compression do not necessarily translate to compression–shear or torsional loading. These experimental findings support selecting radial grading according to the intended loading conditions. The conclusions apply to the tested Digital ABS Plus™ designs and topology–porosity combinations.

Funding Declaration

This project received no external funding.

Declaration of Competing Interest

The authors declare that they have no known competing financial interests or personal relationships that could have appeared to influence the work reported in this paper.

Data availability

Data will be made available on request.

Declaration of generative AI and AI-assisted technologies in the manuscript preparation process

During the preparation of this work the authors used ChatGPT to assist with language editing of the manuscript. After using this tool, the authors reviewed and edited the content as needed and take full responsibility for the content of the published article.

References

[1] B. Ziaie, L. Niu, W. Saleem, L. Ni, M.F. Rathore, X. Velay, Characterization of selective laser melted Ti6Al4V TPMS porous structures for biomedical applications, Journal of Alloys and Compounds 1022 (2025) 180084.
[2] I. Roohani, A. Entezari, H. Zreiqat, Liquid crystal display technique (LCD) for high resolution 3D printing of triply periodic minimal surface lattices bioceramics, Additive Manufacturing 74 (2023) 103720.
[3] F. Liu, Y. Wang, J. Cao, J. Chen, T. Luo, C. Zhou, Y. Tang, H. Xie, A simple method for fabricating polymer/ceramic functionally graded material scaffold, Ceramics International 50(9) (2024) 14497-14512.
[4] I. Maskery, N.T. Aboulkhair, A.O. Aremu, C.J. Tuck, I.A. Ashcroft, Compressive failure modes and energy absorption in additively manufactured double gyroid lattices, Additive Manufacturing 16 (2017) 24-29.
[5] A. du Plessis, N. Razavi, M. Benedetti, S. Murchio, M. Leary, M. Watson, D. Bhate, F. Berto, Properties and applications of additively manufactured metallic cellular materials: A review, Progress in Materials Science 125 (2022) 100918.
[6] E. Maevskaia, J. Guerrero, C. Ghayor, I. Bhattacharya, F.E. Weber, Triply Periodic Minimal Surface-Based Scaffolds for Bone Tissue Engineering: A Mechanical, In Vitro and In Vivo Study, Tissue Eng Part A 29(19-20) (2023) 507-517.

[7] Z. Dong, X. Zhao, Application of TPMS structure in bone regeneration, Engineered Regeneration 2 (2021) 154-162.
[8] I. Roohani, S. Wang, C. Xu, P. Newman, A. Entezari, Y. Lai, H. Zreiqat, Bioinspired Nanoscale 3D Printing of Calcium Phosphates Using Bone Prenucleation Clusters, Advanced Materials 37(13) (2025) 2413626.
[9] F.P.W. Melchels, K. Bertoldi, R. Gabbrielli, A.H. Velders, J. Feijen, D.W. Grijpma, Mathematically defined tissue engineering scaffold architectures prepared by stereolithography, Biomaterials 31(27) (2010) 6909-6916.
[10] Y. Wakjira, A. Cioni, H.G. Lemu, Current status of the application of additive-manufactured TPMS structure in bone tissue engineering, Progress in Additive Manufacturing 10(2) (2025) 1085-1102.
[11] X. Zhou, Y. Jin, J. Du, Functionally Graded Scaffolds with Programmable Pore Size Distribution Based on Triply Periodic Minimal Surface Fabricated by Selective Laser Melting, Materials (Basel) 13(21) (2020).
[12] F. Liu, Z. Mao, P. Zhang, D.Z. Zhang, J. Jiang, Z. Ma, Functionally graded porous scaffolds in multiple patterns: New design method, physical and mechanical properties, Materials & Design 160 (2018) 849-860.
[13] O. Al-Ketan, D.-W. Lee, R. Rowshan, R.K. Abu Al-Rub, Functionally graded and multi-morphology sheet TPMS lattices: Design, manufacturing, and mechanical properties, Journal of the Mechanical Behavior of Biomedical Materials 102 (2020) 103520.
[14] G. Savio, R. Meneghello, G. Concheri, Design of variable thickness triply periodic surfaces for additive manufacturing, Progress in Additive manufacturing 4(3) (2019) 281-290.
[15] L. Yan, A. Entezari, Z. Zhang, J. Zhong, J. Liang, Q. Li, J. Qi, An experimental and numerical study of the microstructural and biomechanical properties of human peripheral nerve endoneurium for the design of tissue scaffolds, Frontiers in Bioengineering and Biotechnology Volume 10 - 2022 (2022).
[16] H. Montazerian, M.G.A. Mohamed, M.M. Montazeri, S. Kheiri, A.S. Milani, K. Kim, M. Hoorfar, Permeability and mechanical properties of gradient porous PDMS scaffolds fabricated by 3D-printed sacrificial templates designed with minimal surfaces, Acta Biomaterialia 96 (2019) 149-160.
[17] N.V. Viet, W. Waheed, A. Alazzam, W. Zaki, Effective compressive behavior of functionally graded TPMS titanium implants with ingrown cortical or trabecular bone, Composite Structures 303 (2023) 116288.
[18] S. Kanwar, S. Vijayavenkataraman, 3D printable bone-mimicking functionally gradient stochastic scaffolds for tissue engineering and bone implant applications, Materials & Design 223 (2022) 111199.
[19] X.-Y. Zhang, X.-C. Yan, G. Fang, M. Liu, Biomechanical influence of structural variation strategies on functionally graded scaffolds constructed with triply periodic minimal surface, Additive Manufacturing 32 (2020) 101015.
[20] J. Thomas, N.A. Alsaleh, M. Ahmadein, A.A. Elfar, H.A. Farouk, K. Essa, Graded cellular structures for enhanced performance of additively manufactured orthopaedic implants, The International Journal of Advanced Manufacturing Technology 130(3) (2024) 1887-1900.
[21] S. Yu, J. Sun, J. Bai, Investigation of functionally graded TPMS structures fabricated by additive manufacturing, Materials & Design 182 (2019) 108021.
[22] J. Zhang, X. Chen, Y. Sun, J. Yang, R. Chen, Y. Xiong, W. Hou, L. Bai, Design of a biomimetic graded TPMS scaffold with quantitatively adjustable pore size, Materials & Design 218 (2022) 110665.
[23] Y. Zamani, G. Amoabediny, J. Mohammadi, H. Seddiqi, M.N. Helder, B. Zandieh-Doulabi, J. Klein-Nulend, J.H. Koolstra, 3D-printed poly(Ɛ-caprolactone) scaffold with gradient mechanical properties according to force distribution in the mandible for mandibular bone tissue engineering, Journal of the Mechanical Behavior of Biomedical Materials 104 (2020) 103638.

[24] H. Wu, L. Chao, Q. Zhang, Y. Yi, C. Jiao, Y. Ye, L. Shen, J. Zhao, G. Wu, C. Wang, Design and 3D printing of ceramic maxillofacial prosthesis with gradient pores based on Voronoi-Tessellation principle, Materials Today Communications 33 (2022) 104559.
[25] S. Lee, D. Choi, J.-H. Shim, W. Nam, Efficacy of three-dimensionally printed polycaprolactone/beta tricalcium phosphate scaffold on mandibular reconstruction, Scientific reports 10(1) (2020) 4979.
[26] S. Nosrati, S.A. Hosseini, O. Rahmani, Bending performance of functionally graded gyroid TPMS bone scaffolds on elastic foundations: an analytical approach for mitigating stress shielding, Applied Physics A 132(3) (2026) 159.
[27] H. Guo, Q. Li, H. Zreiqat, A. Entezari, Emerging technologies for personalised oro-maxillofacial bone regeneration: Design strategies and fabrication techniques, Biomaterials 326 (2026) 123709.
[28] C. Hou, Y. Liu, W. Xu, X. Lu, L. Guo, Y. Liu, S. Tian, B. Liu, J. Zhang, C. Wen, Additive manufacturing of functionally graded porous titanium scaffolds for dental applications, Biomaterials Advances 139 (2022) 213018.
[29] X.-Y. Zhang, G. Fang, S. Leeflang, A.A. Zadpoor, J. Zhou, Topological design, permeability and mechanical behavior of additively manufactured functionally graded porous metallic biomaterials, Acta Biomaterialia 84 (2019) 437-452.
[30] T.T. Dao, M.-C. Ho Ba Tho, Biomechanics of the Musculoskeletal System, Biomechanics of the Musculoskeletal System2014, pp. 1-35.
[31] G. Bergmann, F. Graichen, A. Rohlmann, Hip joint loading during walking and running, measured in two patients, J Biomech 26(8) (1993) 969-90.
[32] L.J. Gibson, Cellular solids, Mrs Bulletin 28(4) (2003) 270-274.
[33] A. Karamanli İ, Investigation on Mechanical Properties of Functional Graded Hybrid TPMS Structures Inspired Bone Scaffolds, Polymers (Basel) 18(2) (2026).
[34] I. Maskery, L. Sturm, A.O. Aremu, A. Panesar, C.B. Williams, C.J. Tuck, R.D. Wildman, I.A. Ashcroft, R.J.M. Hague, Insights into the mechanical properties of several triply periodic minimal surface lattice structures made by polymer additive manufacturing, Polymer 152 (2018) 62-71.
[35] B. Sokollu, O. Gulcan, E.I. Konukseven, Mechanical properties comparison of strut-based and triply periodic minimal surface lattice structures produced by electron beam melting, Additive Manufacturing 60 (2022) 103199.
[36] X.-Y. Zhang, G. Fang, L.-L. Xing, W. Liu, J. Zhou, Effect of porosity variation strategy on the performance of functionally graded Ti-6Al-4V scaffolds for bone tissue engineering, Materials & Design 157 (2018) 523-538.
[37] Y. Xiong, Z. Han, J. Qin, L. Dong, H. Zhang, Y. Wang, H. Chen, X. Li, Effects of porosity gradient pattern on mechanical performance of additive manufactured Ti-6Al-4V functionally graded porous structure, Materials & Design 208 (2021) 109911.
[38] Y.C. Wu, C.N. Kuo, M.Y. Shie, Y.L. Su, L.J. Wei, S.Y. Chen, J.C. Huang, Structural design and mechanical response of gradient porous Ti-6Al-4V fabricated by electron beam additive manufacturing, Materials & Design 158 (2018) 256-265.
[39] C. Han, Y. Li, Q. Wang, S. Wen, Q. Wei, C. Yan, L. Hao, J. Liu, Y. Shi, Continuous functionally graded porous titanium scaffolds manufactured by selective laser melting for bone implants, Journal of the Mechanical Behavior of Biomedical Materials 80 (2018) 119-127.
[40] M. Fousová, D. Vojtěch, J. Kubásek, E. Jablonská, J. Fojt, Promising characteristics of gradient porosity Ti-6Al-4V alloy prepared by SLM process, Journal of the mechanical behavior of biomedical materials 69 (2017) 368-376.

[41] M. Afshar, A.P. Anaraki, H. Montazerian, J. Kadkhodapour, Additive manufacturing and mechanical characterization of graded porosity scaffolds designed based on triply periodic minimal surface architectures, J Mech Behav Biomed Mater 62 (2016) 481-494.
[42] C. Zhang, Z. Jiang, L. Zhao, W. Guo, Z. Jiang, X. Li, G. Chen, Mechanical characteristics and deformation mechanism of functionally graded triply periodic minimal surface structures fabricated using stereolithography, International Journal of Mechanical Sciences 208 (2021) 106679.
[43] C.J. Ejeh, I. Barsoum, R.K. Abu Al-Rub, Flexural properties of functionally graded additively manufactured AlSi10Mg TPMS latticed-beams, International Journal of Mechanical Sciences 223 (2022) 107293.
[44] Y.M. Hailu, A. Nazir, S.-C. Lin, J.-Y. Jeng, The Effect of Functional Gradient Material Distribution and Patterning on Torsional Properties of Lattice Structures Manufactured Using MultiJet Fusion Technology, Materials 14(21) (2021) 6521.
[45] O. Al-Ketan, R.K. Abu Al-Rub, MSLattice: A free software for generating uniform and graded lattices based on triply periodic minimal surfaces, Material Design & Processing Communications 3(6) (2021) e205.
[46] S. Sadoughi, G. Bevill, E.F. Morgan, V. Palepu, T.M. Keaveny, K.A. Wear, Biomechanical structure-function relations for human trabecular bone - comparison of calcaneus, femoral neck, greater trochanter, proximal tibia, and vertebra, Comput Methods Biomech Biomed Engin 26(5) (2023) 508-516.
[47] M. Dr. Stein, S. Feik, C. Thomas, J. Clement, J. Wark, An automated analysis of intracortical porosity in human femoral bone across age, Journal of Bone and Mineral Research 14(4) (1999) 624-632.
[48] X. Li, Y.-Z. Xiong, H. Zhang, R.-N. Gao, Development of functionally graded porous titanium/silk fibroin composite scaffold for bone repair, Materials Letters 282 (2021) 128670.
[49] S.C. Cowin, Bone mechanics handbook, CRC press2001.
[50] K.F. Leong, C.K. Chua, N. Sudarmadji, W.Y. Yeong, Engineering functionally graded tissue engineering scaffolds, J Mech Behav Biomed Mater 1(2) (2008) 140-52.
[51] J.H. Peck, K.D. Kavlock, B.L. Showalter, B.M. Ferrell, D.G. Peck, A.E. Dmitriev, Mechanical performance of lumbar intervertebral body fusion devices: An analysis of data submitted to the Food and Drug Administration, Journal of Biomechanics 78 (2018) 87-93.